Dalton Transactions

ROYAL SOCIETY OF CHEMISTRY

PAPER

View Article Online
View Journal | View Issue

Cite this: *Dalton Trans.*, 2026, **55**, 4421

Incorporating rare-earth samarium into $MnIn_2S_4$ micron flowers for visible-light-driven H_2O_2 generation and organic pollutant degradation

Zhichao Yi,[a] Jianhong Wu,[a] Chensheng Zhou,[a] Zhiquan Lai,[a] Kailian Zhang,[a] Kangqiang Lu,[a] Weiya Huang,[a] Changlin Yu[b] and Kai Yang*[a]

Received 18th December 2025,
Accepted 19th February 2026

DOI: 10.1039/d5dt03035h

rsc.li/dalton

Metal chalcogenide semiconductors show promise for energy conversion and environmental remediation due to their visible-light responsiveness, yet rapid recombination of photogenerated electron–hole pairs limits their practical efficiency. Here, a series of samarium (Sm)-doped $MnIn_2S_4$ photocatalysts were synthesized *via* a one-pot hydrothermal method and systematically explored, and it was found that Sm^{3+} incorporation modulates their structure and photocatalytic performance. Among them, 5% Sm-doped $MnIn_2S_4$ exhibits superior activity, achieving a H_2O_2 production rate of 143 μmol g^{-1} h^{-1}—1.5 times higher than that of the undoped material—and degrading methylene blue with an 89% efficiency and a reaction rate 1.6-fold faster than that of the pristine phase. Mechanistic studies reveal that superoxide radicals ($^{\bullet}O_2^-$) dominate the photocatalytic process, with H_2O_2 formation proceeding *via* a two-electron oxygen reduction pathway. These findings demonstrate an effective strategy for enhancing metal chalcogenides with rare-earth doping and provide guidance for the design of high-performance inorganic photocatalysts.

1. Introduction

Photocatalytic technology, as a green approach for energy conversion and pollution control, can convert solar energy into chemical energy and holds broad application prospects in hydrogen production, hydrogen peroxide synthesis, and degradation of organic pollutants.[1–5] This approach enables the direct conversion of solar energy into chemical energy, with particular significance in hydrogen evolution, hydrogen peroxide synthesis, and degradation of organic pollutants. Among various photocatalytic materials, metal chalcogenide semiconductors have attracted considerable attention due to their suitable band structures and visible-light-responsive characteristics. $MnIn_2S_4$ is a typical I–III–VI group metal sulfide semiconductor with a layered crystal structure similar to $ZnIn_2S_4$.[6,7] Its bandgap of 2.0–2.5 eV endows it with the capacity to harvest approximately 43% of the visible-light region in the solar spectrum. Additionally, its advantages include facile synthesis procedures and high absorption coefficient, rendering it a promising visible-light-responsive photocatalyst.[8–12] However, pure-phase $MnIn_2S_4$ suffers from excessively rapid recombination of photogenerated carriers, with a charge transfer resistance (R_{ct}) as high as 5470 Ω cm^2 and a photocurrent density of only 3.9 μA cm^2, resulting in charge separation and migration efficiencies that are difficult to meet practical catalytic requirements.[13] Even with conventional transition metal doping (such as Ni doping), $MnIn_2S_4$ still fails to form efficient electron traps, maintaining a high charge transfer resistance of 2850 Ω cm^2 and achieving only a modest increase in photocurrent density to 8.2 μA cm^2. The issue of carrier recombination remains fundamentally unresolved.[14] Therefore, it is necessary to explore other metal doping strategies to optimize its electronic structure and enhance carrier separation efficiency.

Rare-earth elements have attracted considerable attention owing to their unique electronic configurations. Their incompletely filled 4f orbitals and empty 5d orbitals allow them to act as electron or hole traps, which effectively suppress the recombination of photogenerated charge carriers and thereby enhance photocatalytic activity.[15–18] Particularly, samarium (Sm^{3+}) ions have shown remarkable capability in modulating the electronic structure of semiconductors through their specific energy level characteristics.[19] Previous studies have indicated that Sm^{3+} doping can effectively narrow the bandgap, improve visible light absorption, and promote charge separation in various semiconductor systems.[20,21] Nevertheless, systematic investigations on the structure–activity relationship of Sm^{3+} doped $MnIn_2S_4$, especially regard-

[a]*School of Chemistry and Chemical Engineering, Jiangxi Provincial Key Laboratory of Functional Crystalline Materials Chemistry, Jiangxi University of Science and Technology, Ganzhou 341000, Jiangxi, China. E-mail: yangkai@jxust.edu.cn*
[b]*School of Chemical Engineering, Guangdong University of Petrochemical Technology, Maoming 525000, Guangdong, China*

ing the doping concentration effects on material properties and photocatalytic mechanisms, remain insufficiently explored.

Based on this, $MnIn_2S_4$ photocatalysts with different molar ratios of Sm doping (Sm doping ratios of 2%, 5%, and 10%) were prepared in this study *via* a one-step hydrothermal method. Their physicochemical properties such as phase, morphology, and electronic structure were systematically characterized. The photocatalytic production of H_2O_2 and degradation of methylene blue were employed as target reactions to investigate the regulatory effect of Sm doping on the photocatalytic performance of $MnIn_2S_4$. The study establishes a clear correlation between Sm^{3+} doping concentration and photocatalytic efficiency, revealing that optimal performance is achieved at a 5% doping level. Furthermore, Sm^{3+} incorporation induces significant morphological modifications and electronic structure adjustments, which collectively contribute to enhancing charge separation efficiency as confirmed by comprehensive photoelectrochemical analysis. Mechanistic investigations identify the superoxide radical ($^{\bullet}O_2^-$) as the primary active species and elucidate the two-electron oxygen reduction pathway for H_2O_2 production. This research provides substantial insights into the design principles of rare-earth-doped metal chalcogenide photocatalysts, advancing the fundamental understanding of structure–activity relationships in modified semiconductor systems. The findings offer practical guidance for developing high-performance photocatalytic materials applicable to sustainable energy conversion and environmental remediation technologies, particularly in the context of solar-driven chemical synthesis and pollutant degradation.

2. Results and discussion

XRD patterns were used to analyze the crystal structure (Fig. 1a). The pure-phase $MnIn_2S_4$ exhibited diffraction peaks at 23.4°, 27.5°, 33.4°, 43.8°, and 47.9°, corresponding to the (220), (311), (400), (511), and (440) crystal planes (JCPDS no. 85-1229), respectively, indicating relatively low crystallinity of the as-prepared sample.[22] After Sm doping, the intensity of the diffraction peaks increased with increasing doping amount, while the peak positions remained unchanged, confirming that Sm^{3+} successfully incorporated into the $MnIn_2S_4$ crystal lattice without altering its crystal structure. FT-IR spectra (Fig. 1b) showed absorption peaks in the range of 1200–1450 cm^{-1}, which were attributed to C–N and C–S bond vibrations, while peaks at 3300–3500 cm^{-1} and 1600–1650 cm^{-1} corresponded to H–O–H stretching vibrations and O–H bending vibrations, respectively.[23,24]

SEM and TEM analyses provide visual evidence for understanding the effect of Sm doping on the microstructure of materials. As observed in Fig. 1c and d, pure $MnIn_2S_4$ was composed of irregular nanosheets self-assembled into microspherical structures, with the nanosheets being relatively thick and having a rough surface. After Sm doping, the nanosheets became significantly thinner and more uniform with a smoother surface. This morphological evolution is conducive to increasing the specific surface area and the number of active sites. The specific surface area of $MnIn_2S_4$ 5%Sm increased to 70.17 $m^2\ g^{-1}$ (Fig. S2), and Table S1 further shows the specific surface area and pore structure parameters. TEM and HRTEM analyses (Fig. 1e and f) further revealed that the $MnIn_2S_4$ 5%Sm sample had clear lattice fringes, with a measured lattice spacing of 0.618 nm corresponding to the (111) crystal plane of cubic-phase $MnIn_2S_4$.[25] Elemental mapping confirmed the uniform distribution of Mn, In, S, and Sm elements in the sample (Fig. 1g).

To gain deeper insight into the chemical states of various elements in the composites, X-ray photoelectron spectroscopy (XPS) was employed to characterize the surface chemistry of the samples. The survey spectrum of the sample (Fig. S3) confirmed the presence of all expected elements. As shown in Fig. 2a, the peaks at 161.1 eV and 162.3 eV for the $MnIn_2S_4$ 5% Sm sample were attributed to S $2p_{3/2}$ and S $2p_{1/2}$, respectively, indicating that sulfur existed in the form of S^{2-} ions.[26] Fig. 2b shows the In 3d XPS spectrum, where peaks at binding energies of 444.3 eV and 451.9 eV are assigned to In $3d_{5/2}$ and In $3d_{3/2}$,[27] respectively, verifying the presence of In^{3+}. As shown in Fig. 2c, the $MnIn_2S_4$ 5%Sm sample exhibits peaks at binding energies of 636.5 eV and 642.1 eV, corresponding to Mn $2p_{3/2}$ and Mn $2p_{1/2}$, respectively.[28] Fig. 2d shows that the $MnIn_2S_4$ 5%Sm sample has peaks at binding energies of 1078.0 eV and 1084.7 eV, which are assigned to Sm $3d_{5/2}$ and Sm $3d_{3/2}$, respectively.[29] The high-resolution XPS analysis reveals a consistent negative shift in the binding energies of Mn (−0.3 eV), In (−0.2 eV), and S (−0.15 eV) in the composite. This uniform shift towards lower binding energies indicates electron transfer from $MnIn_2S_4$ to Sm^{3+}, directly evidencing a strong electronic interaction. The absence of Sm elements in the pure $MnIn_2S_4$ sample indicates that Sm^{3+} has been successfully doped into the $MnIn_2S_4$ lattice. Furthermore, the binding energies of Mn 2p, In 3d, and S 2p orbitals in $MnIn_2S_4$ 5%Sm were slightly lower than those in pure $MnIn_2S_4$, implying a strong interaction between Sm^{3+} and $MnIn_2S_4$.

Photoelectrochemical measurements elucidate Sm doping's impact on photogenerated charge carrier behavior. Transient photocurrent responses characterize photogenerated charge transfer in samples, and the carriers' separation efficiency was determined *via* photocurrent response, electrochemical impedance spectroscopy (EIS) with an amplitude of 5 mV s^{-1}, high frequency of 100 kHz, low frequency of 1 Hz and potential of 0.23 V and Kelvin probe force microscopy (KPFM). The photocurrent test results are shown in Fig. 2e. The order of photocurrent intensity for the composite and pure samples is as follows: $MnIn_2S_4$ 5%Sm > $MnIn_2S_4$ 2%Sm > $MnIn_2S_4$ 10%Sm > $MnIn_2S_4$. Thus, the $MnIn_2S_4$-5%Sm sample exhibited the highest photocurrent response intensity, while the pure sample had a lower current density, indicating poor charge carrier separation efficiency in pure $MnIn_2S_4$. From the EIS Nyquist plots (Fig. 2f), the arc radius of $MnIn_2S_4$ 5%Sm is smaller than that of the pure sample, indicating that Sm

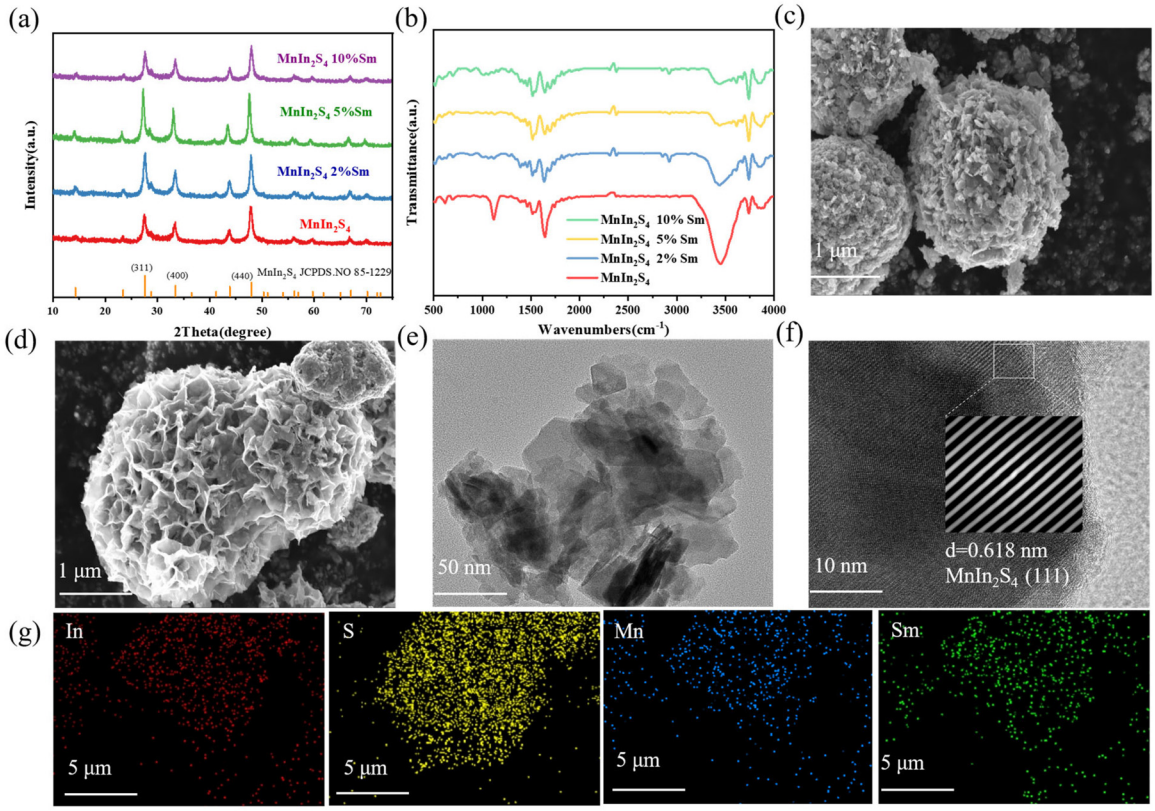

Fig. 1 (a) XRD patterns of all samples; (b) infrared spectra of $MnIn_2S_4$ and composite samples; (c) SEM image of $MnIn_2S_4$; (d) SEM image of $MnIn_2S_4$ 5%Sm; (e and f) TEM and HRTEM images of $MnIn_2S_4$ 5%Sm; and (g) elemental mapping images of $MnIn_2S_4$ 5%Sm.

doping reduced the electron transport resistance, thus facilitating the migration of photogenerated electrons. To quantitatively evaluate Sm regulation on $MnIn_2S_4$ charge transfer, EIS Nyquist plots were fitted *via* the equivalent circuit model, with results summarized in Table S2. The solution resistance (R_s) varies slightly (41.69–51.82 Ω cm^2) across samples, while the charge transfer resistance (R_{ct}) shows a distinct trend: $MnIn_2S_4$ exhibits a high R_{ct} of 5010 Ω cm^2, which drops to 1200 Ω cm^2 (23.9% of the pure counterpart) at 5% Sm doping. Correspondingly, the constant phase element (CPE) with Sm regulation shows a lower value. These results confirm that 5% Sm doping is the optimal ratio for minimizing R_{ct} and boosting charge transfer efficiency. Steady-state photoluminescence (PL) spectra show that $MnIn_2S_4$ 5%Sm has the lowest emission intensity, indicating the highest charge carrier separation efficiency (Fig. 2g). The surface potentials of $MnIn_2S_4$ and $MnIn_2S_4$ 5%Sm measured by KPFM are 145 mV and 209 mV, respectively (Fig. 2h and i). The surface potential of $MnIn_2S_4$ 5%Sm is nearly 1.5 times higher than that of pure $MnIn_2S_4$, demonstrating that Sm doping induced a stronger surface potential, thereby promoting more efficient charge separation.[30] As revealed by ultraviolet-visible diffuse reflectance spectroscopy (UV-Vis DRS), Sm doping effectively narrows the band gap to 2.06 eV, thereby enhancing the visible-light absorption capacity (Fig. S4). In light of the analysis of results derived from Mott–Schottky (MS) measurement, linear sweep voltammetry (LSV) and cyclic voltammetry (CV) tests (Fig. S5–S7), the conduction band position of Sm^{3+}-doped $MnIn_2S_4$ undergoes a negative shift. The double-layer capacitance (C_{dl}) —calculated from the slope of Fig. S7—reflects the electrochemically active surface area: $MnIn_2S_4$ has a low C_{dl} value (0.74 mF cm^{-2}), while $MnIn_2S_4$ 5%Sm shows a 6.4-fold higher C_{dl} value (4.71 mF cm^{-2}), indicating the expanded electrochemically active surface area (ECSA) that aids material–electrolyte charge interaction. These results (the minimized R_{ct} and the enlarged C_{dl}) confirm that 5% Sm doping is optimal for charge transfer efficiency, aligning with transient photocurrent and PL trends. This shift not only facilitates the separation of photogenerated electron–hole pairs in $MnIn_2S_4$ but also enhances its reduction capability.

The photocatalytic performance was evaluated based on H_2O_2 production capacity. As shown in Fig. 3a, $MnIn_2S_4$ produces only a small amount of H_2O_2, whereas Sm-doped samples exhibit significantly enhanced H_2O_2 production. $MnIn_2S_4$ 5%Sm achieves the optimal performance with a maximum H_2O_2 production rate of 143 μmol g^{-1} h^{-1}, which is approximately 1.5 times higher than that of $MnIn_2S_4$. Contact angle tests indicate that $MnIn_2S_4$ 5%Sm has a significantly lower contact angle than the pure sample, suggesting enhanced hydrophilicity that facilitates the diffusion and adsorption of reactants on the catalyst (Fig. S8). The enhanced hydrophilicity in H_2O_2-producing catalyst primarily boosts per-

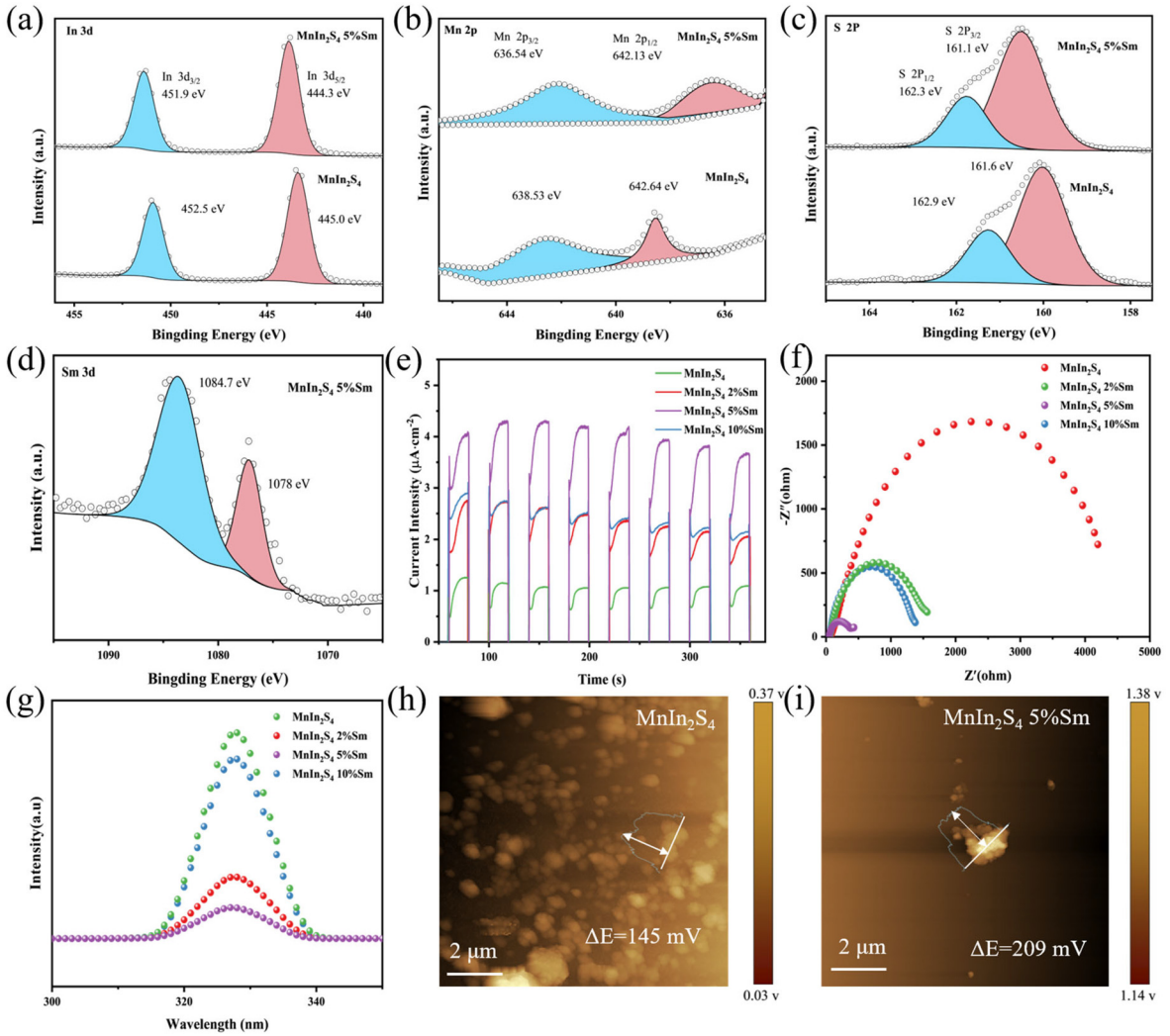

Fig. 2 XPS spectra of the sample: (a) In 3d; (b) S 2p; (c) Mn 2p; and (d) Sm 3d; (e) photocurrent diagram; (f) AC impedance diagram; (g) fluorescence spectrum; (h) surface potential diagram of $MnIn_2S_4$; and (i) surface potential diagram of $MnIn_2S_4$ 5%Sm.

formance by improving mass transfer and optimizing the interfacial reaction environment. It facilitates better infiltration of water and dissolved oxygen at catalytic sites, promoting an efficient oxygen reduction reaction (ORR) *via* a direct two-electron pathway. This modification effectively enhanced the H_2O_2 production activities of photocatalysts.

To elucidate the reaction mechanism, free radical trapping experiments were conducted by adding isopropanol (IPA, $^{\bullet}OH$ scavenger), EDTA-2Na (h^+ scavenger), and *p*-benzoquinone (P-BQ, $^{\bullet}O_2^-$ scavenger) to the reaction system. The addition of P-BQ drastically reduces the H_2O_2 production rate from 143 to 71 μmol g^{-1} h^{-1} within 120 min, indicating that $^{\bullet}O_2^-$ serves as the primary active species. The addition of IPA also decreases the H_2O_2 yield from 143 to 104 μmol g^{-1} h^{-1}, suggesting that the hydroxyl radical ($^{\bullet}OH$) acts as a secondary active species (Fig. 3b).

The recyclability of $MnIn_2S_4$ 5%Sm for H_2O_2 production was investigated over four consecutive cycles. Under Xe lamp irradiation, the H_2O_2 yield remains at 120.1 μmol g^{-1} h^{-1}, demonstrating good catalytic stability (Fig. 3c). XRD (Fig. S9), XPS (Fig. S10) and BET (Fig. S11) characterization studies were further conducted on the as-prepared samples before and after the reaction to evaluate their structural and textural stability. All the characterization results demonstrated that the material exhibited no obvious structural, compositional or textural variations after the reaction, which sufficiently verifies the excellent cycling stability of the as-synthesized material. Furthermore, the photocatalytic activity was assessed by degrading methylene blue (MB) as the target pollutant. After 100 minutes of visible light irradiation, the degradation rates of 20 ppm MB by pure $MnIn_2S_4$ and the Sm-doped samples (2%, 5%, and 10%) are 70%, 79%, 89%, and 80%, respectively (Fig. 3d). Reaction kinetic fitting confirms that $MnIn_2S_4$-5%Sm has the fastest degradation kinetics (Fig. 3e). $MnIn_2S_4$ 5%Sm maintains 82% of its initial degradation efficiency after four cycles, confirming its excellent cycling stability (Fig. 3f).

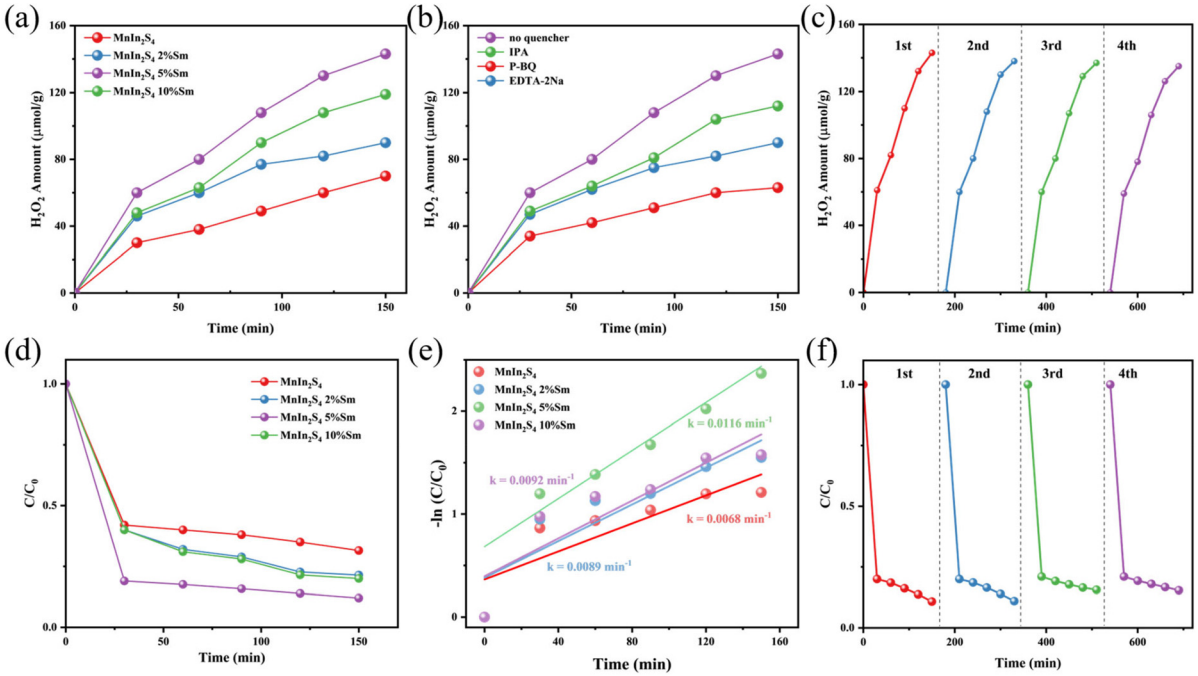

Fig. 3 (a) Activity graph of photocatalytic H_2O_2 production; (b) reaction activity trapping experiment; (c) H_2O_2 production cycle experiment of $MnIn_2S_4$ 5%Sm; (d) photocatalytic degradation activity graph of methylene blue; (e) reaction kinetics fitting graph; and (f) degradation cycle experiment of methylene blue by $MnIn_2S_4$ 5%Sm.

To identify the primary active species and clarify the reaction mechanism of photocatalytic H_2O_2 production, electron spin resonance (ESR) measurements were performed to detect the presence of $^{\bullet}OH$ and $^{\bullet}O_2^-$ during the reaction. 5,5-Dimethyl-1-pyrroline *N*-oxide (DMPO) was used as the spin trap agent and dissolved in methanol/water mixtures to capture the generated radicals, and ESR signals were recorded before and after light irradiation.[31–33] As shown in Fig. 4a and b, under dark conditions, no ESR signals for DMPO–$^{\bullet}OH$ and DMPO–$^{\bullet}O_2^-$ are detected for either the $MnIn_2S_4$ or $MnIn_2S_4$ 5%Sm catalyst. After Xe lamp irradiation, distinct ESR signals of $^{\bullet}OH$ and $^{\bullet}O_2^-$ appear, and their intensities increase with a prolonged irradiation time, indicating the accumulation of these radicals on the catalyst surface.

More crucially, compared to pure $MnIn_2S_4$, $MnIn_2S_4$ 5%Sm exhibits higher signal intensities in the detection of both $^{\bullet}OH$ and $^{\bullet}O_2^-$ radicals. More importantly, $MnIn_2S_4$ 5%Sm exhibits higher signal intensities of both $^{\bullet}OH$ and $^{\bullet}O_2^-$ than pure $MnIn_2S_4$, with a more significant increase in $^{\bullet}O_2^-$ intensity than that of $^{\bullet}OH$. This result suggests that $^{\bullet}O_2^-$ is the dominant active species, while $^{\bullet}OH$ plays a secondary role in the catalytic process. Collectively, the trapping experiments and ESR spectra confirm that $MnIn_2S_4$ 5%Sm enhances the generation of $^{\bullet}O_2^-$ and $^{\bullet}OH$ photocatalytically active species, thus improving H_2O_2 production efficiency.

To further clarify the H_2O_2 formation mechanism of $MnIn_2S_4$ 5%Sm, *in situ* diffuse reflectance infrared Fourier transform spectroscopy (*in situ* DRIFTS) was used to monitor the reaction intermediates under illumination.[34] As shown in Fig. 4c, under dark conditions, $MnIn_2S_4$ 5%Sm maintains an adsorption–desorption equilibrium of O_2 within the first 30 minutes. Subsequently, under continuous illumination, the peak intensity around 950–1000 cm^{-1} corresponds to the O–O bond. Additionally, the peak at around 1100 cm^{-1} gradually intensifies, which is attributed to the superoxide radical ($^{\bullet}O_2^-$). The gradual enhancement of the $^{\bullet}O_2^-$ peak (1090 cm^{-1}) and the $^{\bullet}OOH$ peak in the range of 1200 cm^{-1} to 1300 cm^{-1} further confirms the involvement of the two-step single-electron reduction pathway.[35,36] The corresponding 2D color mapping contour plot directly visualizes the dynamic generation and evolution of characteristic wavenumber signals of H_2O_2, $^{\bullet}OOH$ and other reactive oxygen species with reaction time (Fig. 4d). Therefore, the mechanism for H_2O_2 synthesis in $MnIn_2S_4$ 5% Sm confirms the two-electron oxygen reduction pathway ($O_2 + e^- \rightarrow {}^{\bullet}O_2^- + H^+ \rightarrow {}^{\bullet}OOH + e^- + H^+ \rightarrow H_2O_2$).

The concentrations of $^{\bullet}O_2^-$ and $^{\bullet}OH$ were quantified using the absorbance spectra of the nitroblue tetrazolium (NBT) (Fig. 5(a)) and the fluorescence spectra of 7-hydroxycoumarin (Fig. 5(b)), respectively. After 2.5 hours of visible-light irradiation, the concentration of $^{\bullet}O_2^-$ generated by $MnIn_2S_4$ 5%Sm reaches 5.7 μM, while that of $^{\bullet}OH$ is 4.8 μM, which confirms that $^{\bullet}O_2^-$ is the primary active species in the system (Fig. 5(c)). The capturing experiment (Fig. 5(d)) shows that the MB degradation efficiency drops sharply from 89% to 18% after adding *p*-benzoquinone (P-BQ, the $^{\bullet}O_2^-$ scavenger), while it only decreases to 61% after adding isopropanol (IPA, the $^{\bullet}OH$ scavenger).[37,38] Combined with the quantitative data of active species, this indicates that $^{\bullet}O_2^-$ is the dominant active species for MB degradation, with photogene-

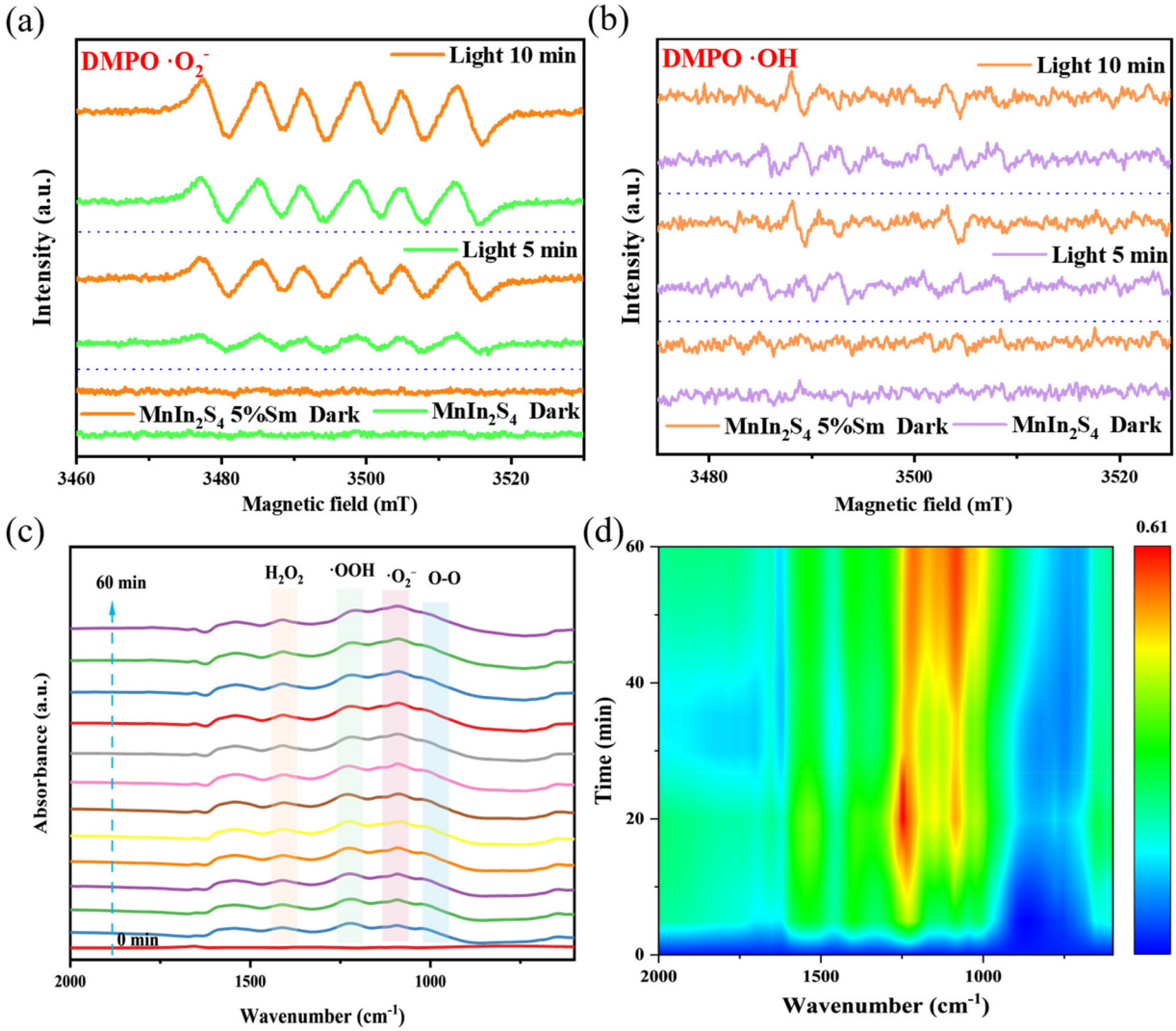

Fig. 4 ESR signals of $MnIn_2S_4$ and $MnIn_2S_4$ 5%Sm under dark and light conditions: (a) DMPO$^{\bullet}O_2^-$; (b) DMPO$^{\bullet}$OH; (c) *in situ* diffuse reflectance infrared absorption spectrum of $MnIn_2S_4$ 5%Sm; (d) and the corresponding 2D color mapping.

rated electrons driving the generation of $^{\bullet}O_2^-$ *via* oxygen reduction as the core pathway, and the material reacts with H_2O_2 to generate $^{\bullet}$OH, playing a minor role.[39]

Integrating the above characterization and spectral analyses, a comprehensive photocatalytic mechanism for Sm^{3+}-doped $MnIn_2S_4$ is proposed, as illustrated in Fig. 6. Upon visible-light irradiation, $MnIn_2S_4$ semiconductors can induce the generation of free charge carriers (conduction band electrons and valence band holes). The introduction of Sm^{3+} can narrow the band gap width of pristine $MnIn_2S_4$, which not only broadens the visible-light absorption range but also facilitates the rapid separation of photogenerated electron–hole pairs by reducing the separation and transport efficiency of photo-generated carriers, thereby achieving high-efficiency charge separation. From a thermodynamic perspective, the conduction band edge potential of $MnIn_2S_4$ 5%Sm (−0.445 eV *vs.* NHE) is substantially more negative than the standard redox potential of the $O_2/^{\bullet}O_2^-$ couple (−0.33 V *vs.* NHE). O_2 molecules are adsorbed on the active sites of the catalyst, and the photogenerated electrons in the conduction band are transferred to the antibonding orbitals of the adsorbed O_2 molecules, breaking the electronic balance of O_2 and ultimately generating $^{\bullet}O_2^-$, with the reaction formula: $O_2 + e^- \rightarrow {}^{\bullet}O_2^-$. These $^{\bullet}O_2^-$ radicals serve as the core active species for H_2O_2 production *via* the two-electron reduction pathway. As confirmed by the two-electron oxygen reduction pathway, the generated $^{\bullet}O_2^-$ first undergoes protonation to form $^{\bullet}$OOH, and then receives another photogenerated electron and proton to generate H_2O_2 ($O_2 + e^- \rightarrow {}^{\bullet}O_2^-$, $^{\bullet}O_2^- + H^+ \rightarrow {}^{\bullet}$OOH, $^{\bullet}$OOH + e^- + $H^+ \rightarrow H_2O_2$). The conduction band potential of Sm-$MnIn_2S_4$ is −0.445 eV *vs.* NHE, which is more negative than the standard redox potential of $H_2O_2/^{\bullet}$OH (0.87 eV *vs.* NHE), making the single-electron reduction of H_2O_2 by photogenerated electrons thermodynamically feasible: $H_2O_2 + e^- \rightarrow {}^{\bullet}OH + OH^-$.

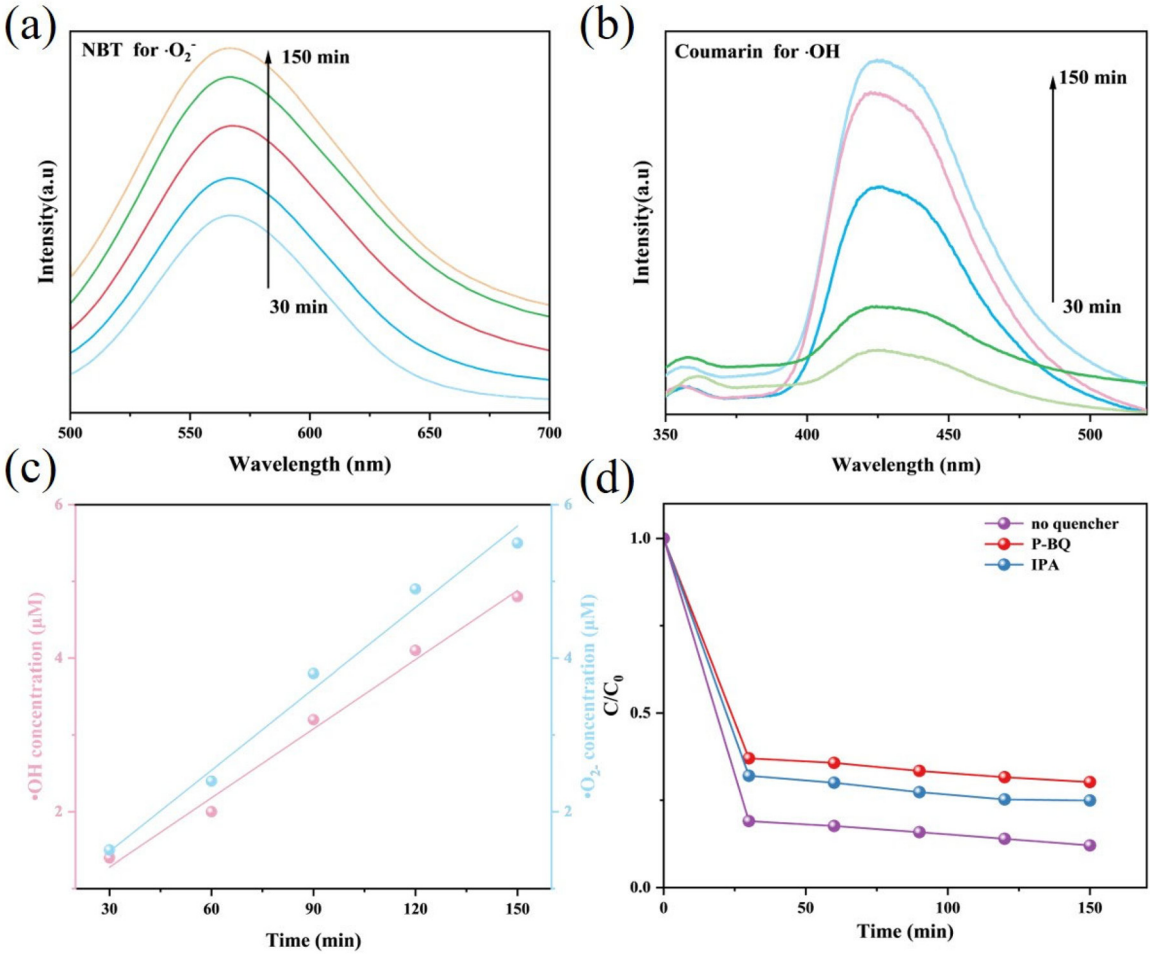

Fig. 5 (a) NBT-based UV absorption spectra of $^{\bullet}O_2^-$ over $MnIn_2S_4$ 5%Sm with varied illumination durations; (b) fluorescence spectra of 7-hydroxycoumarin over Sm-$MnIn_2S_4$ under visible-light irradiation; (c) time-dependent photocatalytic yields of $^{\bullet}O_2^-$ and $^{\bullet}OH$ ([NBT] = 1 mM, [7-hydroxycoumarin] = 1 mM, [catalyst] = 0.4 mg mL^{-1}); and (d) capturing experiments for MB degradation.

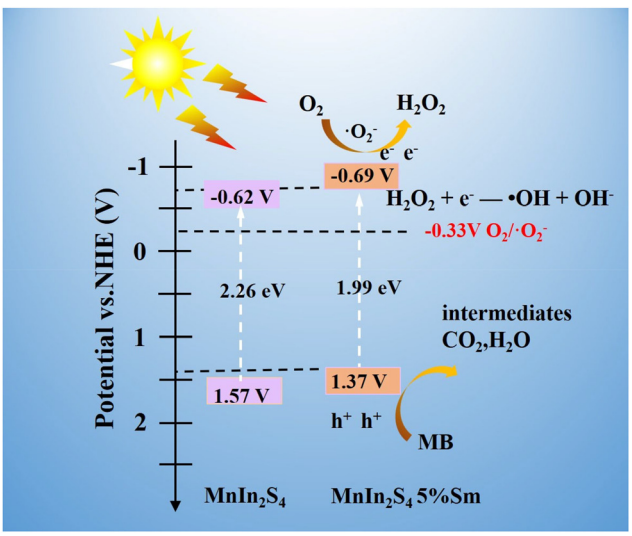

Fig. 6 Mechanism diagram of H_2O_2 production *via* photocatalysis by $MnIn_2S_4$ 5%Sm.

3. Conclusion

In this study, Sm-doped $MnIn_2S_4$ photocatalysts were successfully prepared *via* a one-step hydrothermal method, and their photocatalytic performance and underlying mechanism were systematically investigated. The $MnIn_2S_4$ 5%Sm sample exhibited superior photocatalytic activity, with an H_2O_2 production rate of 143 μmol g^{-1} h^{-1} (1.5 times that of pure $MnIn_2S_4$) and an MB degradation rate of 89%. Characterization results revealed that Sm^{3+} doping refines the material morphology, increases the specific surface area to 70.17 m^2 g^{-1}, narrows the bandgap, and enhances the separation and migration of photogenerated charge carriers. Mechanistic studies confirmed that $^{\bullet}O_2^-$ is the main active species, and H_2O_2 is produced *via* a two-electron oxygen reduction pathway. This study provides certain ideas and insights for the design of rare-earth-doped modified sulfide materials for applications in the fields of photocatalytic hydrogen peroxide production and pollutant treatment.

Conflicts of interest

There are no conflicts of interest to declare.

Data availability

The additional data supporting this article have been included as part of the supplementary information (SI). Supplementary information: chemicals required, material characterisation, photocatalytic H_2O_2 production and pollutant degradation, flowchart of hydrothermal synthesis, N_2 adsorption–desorption analysis plot, XPS full spectrum, UV-Vis diffuse reflectance spectra, Mott–Schottky plots, LSV diagrams, cyclic voltammetry curves, and contact angles. See DOI: https://doi.org/10.1039/d5dt03035h.

Acknowledgements

This work received financial support from multiple funding agencies, including the National Natural Science Foundation of China (No. 22366018, 5236005, 22462010, 22272034, and 22578080), the Key Projects of Jiangxi Provincial Natural Science Foundation (No. 20232ACB203022, and 20224ACB213010), the Jiangxi Province 'Double Thousand' Talent Training Plan (No. jxsq2023201086, jxsq2023102141, jxsq2023102142, jxsq2023102143 and jxsq2023102196) and Jiangxi Provincial Key Laboratory of Functional Crystalline Materials Chemistry (No. 2024SSY05161), Program of Qingjiang Excellent Young Talents at JXUST (No. JXUSTQJBJ2020005), the PhD Startup Fund of Jiangxi University of Science and Technology (No. jxust-124) and the Jiangxi Provincial Natural Science Foundation (No. 20252BAC240238, 20252BAC220013 and 20224BAB203018).

References

1 F. Y. Yu, Y. J. Zhou, H. Q. Tan, Y. G. Li and Z. H. Kang, *Adv. Energy Mater.*, 2023, **13**, 2300119.
2 T. Wang, H.-J. Wang, J.-S. Lin, J.-L. Yang, F.-L. Zhang, X.-M. Lin, Y.-J. Zhang, S. Jin and J.-F. Li, *Chin. J. Struct. Chem.*, 2023, **42**, 100066.
3 Y. Wang, J. A. Torres, M. Shviro, M. Carmo, T. He and C. Ribeiro, *Prog. Mater. Sci.*, 2022, **130**, 100965.
4 Z. An, G. Ma, Y. Yang, W. Wang, Y. Wang, S. Tian, J. Gao, X. Gong, F. Guo and J. Tang, *J. Mater. Chem. A*, 2025, **13**, 31954–31977.
5 F. Wang, M. Zhou, W. Huang, K. Lu, S. Ouyang, W. Xiang, C. Zhou, C. Yu and K. Yang, *Inorg. Chem. Front.*, 2024, **11**, 4297–4306.
6 J. Di, C. Chen, C. Zhu, X. Cao, J. Xiong, R. Long, S. Li, W. Jiang and Z. Liu, *Small*, 2024, **20**, 2402808.
7 F. Wang, Y. Yang, X. Li, W. Huang, K. Lu, S. Ouyang, W. Xiang, C. Zhou, C. Yu, M. Zhou and K. Yang, *J. Environ. Chem. Eng.*, 2024, **12**, 114788.
8 H. Wang, X. Tang, Y. Sun, Z. Huang and L. Zhao, *Chem. Eng. J.*, 2024, **480**, 148308.
9 Y. Wang, Y. Liu, F. Tian, S. Bao, C. Sun, W. Yang and Y. Yu, *J. Colloid Interface Sci.*, 2022, **625**, 264–277.
10 Y. Wang, L. Qiu, S. Bao, F. Tian, L. He, W. Yang, Y. Liu and Y. Yu, *Chem. Eng. J.*, 2023, **468**, 143768.
11 Y. Chen and L. Zhang, *Appl. Catal., B*, 2024, **347**, 123768.
12 L. Wang, X. Fu, C. Zhu, X. Xiao, Y. Xu, W. Huang, Z. He, Y. Xia, T. Yang and Y. Gao, *Sep. Purif. Technol.*, 2025, **355**, 129712.
13 S. Wang, L. Xie and L. Li, *J. Mater. Chem. C*, 2022, **10**, 17245–17254.
14 Y. Liu, S. Chen and W. Huang, *J. Alloys Compd.*, 2025, **1063**, 186247–186256.
15 L. Sun, X. Liu, Y. Feng, X. Ding, J. Wang, N. Jiang and S. Wang, *Appl. Catal., B*, 2023, **338**, 122979.
16 N. A. Mohamed, T. S. Kiong and A. F. Ismail, *Coord. Chem. Rev.*, 2025, **543**, 216917.
17 H. Zou, Y. Qi, S. Du, Y. Bao, X. Xin, W. Fan, Y. Xiao, S. Jin, Z. Feng and F. Zhang, *J. Am. Chem. Soc.*, 2024, **146**, 28182–28189.
18 F. Zhou, Y. Zhang, J. Wu, W. Yang, X. Fang, T. Jia, Y. Ling, P. He, Q. Liu and J. Lin, *Appl. Catal., B*, 2024, **341**, 123347.
19 P. Pascariu, C. Cojocaru, M. Homocianu and P. Samoila, *J. Environ. Manage.*, 2022, **316**, 115317.
20 R. Guo, X. Zhang, Y. Chen and Y. Zhang, *Adv. Funct. Mater.*, 2024, **34**, 2408838.
21 P. Wang, J. Luo, B. Liu, H. Ren, J. Zhao, H. Guo and C. Wang, *Chem. Eng. J.*, 2025, **510**, 161834.
22 W. Li, X. Lv, Y. Wang, Q. Li, R. Song and X. Yang, *J. Alloys Compd.*, 2025, **1048**, 185242.
23 D. Liu, L. Jiang, D. Chen, Z. Hao, B. Deng, Y. Sun, X. Liu, B. Jia, L. Chen and H. Liu, *Chem. Eng. J.*, 2024, **482**, 149165.
24 F. Wang, X. Li, K. Lu, M. Zhou, C. Yu and K. Yang, *Chin. J. Catal.*, 2024, **63**, 190–201.
25 Z. Ji, Y. Fan, W. Li, Y. Jin, N. Lei, Z. Li and X. Zhong, *J. Mater. Chem. C*, 2025, **13**, 18824–18837.
26 X. Zhang, Z. Cheng, P. Deng, L. Zhang and Y. Hou, *Int. J. Hydrogen Energy*, 2021, **46**, 15389–15397.
27 Y. Ma, Z. Zhang, X. Jiang, R. Sun, M. Xie and W. Han, *J. Mater. Chem. C*, 2021, **9**, 3987–3997.
28 C.-C. Lin, T.-R. Liu, S.-R. Lin, K. M. Boopathi, C.-H. Chiang, W.-Y. Tzeng, W.-H. C. Chien, H.-S. Hsu, C.-W. Luo, H.-Y. Tsai, H.-A. Chen, P.-C. Kuo, J. Shiue, J.-W. Chiou, W.-F. Pong, C.-C. Chen and C.-W. Chen, *J. Am. Chem. Soc.*, 2022, **144**, 15718–15726.
29 R. Zhao, C. Chen, Y. Xu, Y. Qu, P. Yu and Y. Wang, *Chem. Eng. J.*, 2025, **524**, 169023.
30 Q. Yu, S. Sun, X. Jin, R. Yan, B. He, N. Sirotkin, A. Agafonov, X. Xiong and K. Lv, *Chin. J. Struct. Chem.*, 2025, **44**, 100620.
31 D. Li, J. Huang, R. Li, P. Chen, D. Chen, M. Cai, H. Liu, Y. Feng, W. Lv and G. Liu, *J. Hazard. Mater.*, 2021, **401**, 123257.

32 Z. Li, C. Wen, D. Li, Z. Fang, Z. Lin, D. Liu, Y. Wang, X. Zhang, P. Chen, W. Lv and G. Liu, *Chem. Eng. J.*, 2024, **492**, 152449.
33 X. K. Li, R. Yang, L. Zou, S. Z. Zheng, M. S. Chen, J. Wen, H. Zhang, C. Wu, Y. C. Zhang and Y. T. Zhou, *Adv. Mater.*, 2024, **37**, 2416283.
34 Y. Lin, Y. Wang, Z. Feng, Y. Gui and L. Liu, *J. Colloid Interface Sci.*, 2025, **682**, 381–391.
35 R. Ji, Y. Dong, X. Sun, C. Pan, Y. Yang, H. Zhao and Y. Zhu, *Appl. Catal., B*, 2024, **349**, 123884.
36 Y. Zhao, X. Li, X. Fan, H. Wang, Y. Liu, Y. Chen, T. Yang, J. Ye, H. Huang, H. Li, X. Zhang, Y. Liu, H. Lin, Y. Zhao and Z. Kang, *Appl. Catal., B*, 2022, **314**, 121499.
37 L.-W. Wei, M.-W. Zheng, S.-H. Liu, H. P. Wang, Y.-C. Pu and V.-C. Nguyen, *Chem. Eng. J.*, 2024, **487**, 150712.
38 L.-W. Wei, S.-H. Liu, V.-C. Nguyen, M.-W. Zheng and H. P. Wang, *Appl. Catal., B*, 2025, **361**, 124594.
39 Y. Deng, W. Liu, R. Xu, R. Gao, N. Huang, Y. Zheng, Y. Huang, H. Li, X. Y. Kong and L. Ye, *Angew. Chem., Int. Ed.*, 2024, **63**, e202319216.